Wideband Sparse Signal Acquisition With Dual-rate Time-Interleaved Undersampling Hardware and Multicoset Signal Reconstruction Algorithms

Thomas Moon, *Member, IEEE*, Hyun Woo Choi, *Member, IEEE*, Nicholas Tzou, and Abhijit Chatterjee, *Fellow, IEEE*

***Abstract*—A new undersampling-based dual-rate signal acquisition technique for measuring a wideband sparse signal (i.e., a multiband signal) is presented in this paper. The proposed architecture employs a combination of dual-rate time-interleaved undersampling hardware and associated multicoset back-end signal processing algorithms. In dual-rate sampling hardware, a pair of uniform samplers is used to acquire a common incoming wideband sparse signal while the operation frequencies of the two samplers have a small frequency offset. Due to the sampling frequency offset, the time grids of the samples obtained from the two samplers are irregularly spaced. These nonuniform periodic samples are then digitally re-sequenced and applied as input to a multicoset signal reconstruction algorithm. The multicoset signal reconstruction algorithm uses the re-sequenced nonuniform periodic samples to achieve a perfect reconstruction of the original wideband signal with an enhanced time resolution beyond the sampling hardware's capability. Compared to the conventional multi-channel sampling approach commonly used with multicoset algorithms, the proposed method uses fewer sampling channels and does not require their accurate clock phase adjustment.**

***Index Terms*— Nonuniform sampling, signal reconstruction, spectral analysis, eeconstruction algorithms, wideband, RF signals.**

I. Introduction

NONUNIFORM periodic undersampling techniques have recently been investigated for the purpose of digitally enhancing the time resolution of sampling-based measurement systems given upper limits of their sampling rates by using associated signal reconstruction algorithms, yielding results even better than the effective sampling rate that can be achieved from conventional time-interleaved sampling methods [1]–[16]. Such a technique is used for the acquisition of high-frequency signal components that are sparse in a certain domain, mostly in the frequency domain, when it is not possible to sample such high-frequency components at the Nyquist rate because of the sampling rate limitation of the sampling hardware being used.

Nonuniform periodic undersampling requires a certain degree of modification to the existing sampling hardware. For instance, multicoset sampling hardware, which is one of various nonuniform periodic undersampling techniques, uses multiple sampling modules configured in parallel with the same sampling frequency but different phases, and each sampling module individually acquires a common analog input signal at nonuniform phases [4], [6]. In [13], a random demodulator consisting of a frequency mixer that uses a pseudo-random bit generator as a substitute for a local oscillator is used as a random modulation front-end to sampling hardware. In [12], a random sampling time-base fed to a sampler to enable random switching between multiple time-interleaved sampler outputs is used as a random front-end. However, in these methods, additional hardware components are used for sampling randomization, which potentially introduce additional measurement noise to the signal acquisition system because of mismatches among sampling devices or the increased timing jitter of the sampling time-base because of the randomization effort.

To overcome difficulties in implementing nonuniform periodic sampling hardware and to minimize the potential increase of sampling noise caused by nonidealities of the nonuniform periodic undersampling hardware, the authors in [8], [16] introduce a multi-rate sampling technique that does not use random sampling hardware or multiple (on the order of 10) analog-to-digital converters. In the multi-rate sampling approach, a smaller number of uniform samplers are used to acquire a common incoming analog signal when the operation frequencies of the samplers have a small frequency offset; hence, it is called multi-rate sampling. For digital signal post-processing of the dual-rate sampled data, a sparsity optimization based inversion algorithm is used, which is a standard use case in compressive sensing [2], [4]–[9]. However, such signal reconstruction algorithms are difficult to implement in digital signal processing devices due to their complexity, and the multi-rate sampling hardware still requires multiple high-speed samplers (if not on the order of 10) and their synchronization, which is an additional burden on system design and a potential cause of increased sampling noise in the hardware. In many blind reconstruction works, the combination of sparse sensing and multicoset sampling is widely used. In sparse sensing, the support of a sampled signal is found by two

Manuscript received April 19, 2014; revised May 20, 2015 and July 29, 2015; accepted July 30, 2015. Date of publication August 18, 2015; date of current version November 10, 2015. The associate editor coordinating the review of this manuscript and approving it for publication was Prof. Zhiyuan Yan. This work was supported in part by Samsung Electronics and by the U.S. National Science Foundation under Award 1421353.

T. Moon, N. Tzou, and A. Chatterjee are with the Department of Electrical and Computer Engineering, Georgia Institute of Technology, Atlanta, GA 30318 USA (e-mail: tmoon@gatech.edu; nltzou@gmail.com; abhijit.chatterjee@ece.gatech.edu).

H. W. Choi is with Nvidia Corporation, Santa Clara, CA 95051 USA (e-mail: hyun@gatech.edu).

Color versions of one or more of the figures in this paper are available online at http://ieeexplore.ieee.org.

Digital Object Identifier 10.1109/TSP.2015.2469648

1053-587X © 2015 IEEE. Personal use is permitted, but republication/redistribution requires IEEE permission.
See http://www.ieee.org/publications_standards/publications/rights/index.html for more information.

of the most popular algorithms that compute sparse signal representations: matching pursuit (MP) [16], [17] and basis pursuit (BP) [18], [19]. In MP, a signal representation is iteratively and greedily found by choosing the atom that maximally improves the representation. Alternately, BP seeks a representation that minimizes the L-1 norm of the coefficients. Once the support of the signal is found, the signal is recovered by a multicoset algorithm. Previously, multicoset signal reconstruction algorithms were used only with the time-offset-based hardware that generates multicoset sampling patterns by applying different time offsets to each channel [20] or with a random-modulated wideband receiver [21]–[23]. As these types of architecture require a large number of samplers and accurate delay circuits with fine resolution or wideband mixers, multicoset sampling architectures were not widely used in the testing and measurement field.

A. Comparisons to Prior Works

To alleviate the practical concerns and cost of the conventional multicoset sampling, we propose a dual-rate sampling hardware system consisting of only two sampling modules to implement nonuniform periodic sampling. The use of a dual-rate sampler reduces additional sampling noise that may be introduced by hardware non-idealities or configuration mismatches among multiple samplers, which in turn compromises the signal integrity of signal acquisition systems.

In this section, the propose work is compared with the prior works on blind multiband signal reconstruction.

Random Demodulator and Modulated Wideband Converter (MWC) [13], [24]: In this approach, the signal is modulated by mixers in an analog front-end (a single channel in [13] and a bank of modulators in [24]) to alias the spectrum into a baseband. Then, the signal is reconstructed by solving the infinite measurement vectors (IMV) problem. However, the quality of the reconstruction is limited by the front-end RF components. The real mixer can create unwanted harmonics in the output and power leakage from the local oscillator (LO) side. Moreover, the calibration is another difficult issue in the MWC scheme due to the many-channel (20–100 channels) presence. In our work, the signal is directly sampled by an ADC without analog pre-processing. Only two channels are required to perform the reconstruction and therefore the calibration process is much easier and less time-consuming.

Delayed-based Multicoset [2]: This work mainly focuses on the spectral support sensing problem, and assumes that the multicoset sample is acquired by an ideal delay module for each channel. In their simulated example, 16 channels are required to reconstruct a 6.3 GHz bandwidth signal. A practical delay module, however, has a limited dynamic range and step size. In our work, the dual-rate sampler is proposed to avoid the use of the delay modules.

Synchronous and Asynchronous Multirate Sampling [8], [25]: In these works, multirate sampling architectures are proposed. The multirate scheme can be classified into two groups by phase synchronization. The proposed work belings to the synchronous multirate sampling category. In [8], synchronous multirate sampling is used to detect the active signal bands location. The full signal reconstruction, however, is not proposed in this work. Moreover, the phase synchronization between the channels is assumed to be given. In [25], the phase synchronization is relaxed to be asynchronous, and both active bands sensing and signal characterization are presented. However, the signal characterization relies on the statistical estimation (cross-correlation between the multirate samples and total variation), which may cause incorrect results due to spectral aliasing and noise. The proposed work fully reconstructs the signal in the presence of spectral aliasing and noise. We also propose an all-digital phase-synchronization scheme for the multirate sampler.

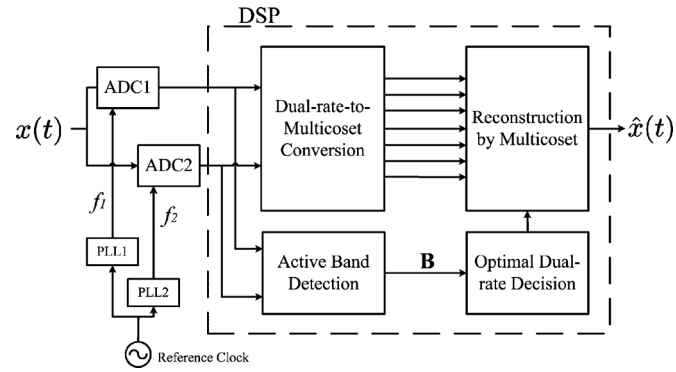

Fig. 1. Block diagram of the proposed dual-rate time-interleaved undersampling and multicoset signal reconstruction.

In Section II, we provide details of the proposed dual-rate time-interleaved undersampling technique and the revised use of the multicoset signal reconstruction algorithm for dual-rate sampled data. The methodology of detecting the active band of the signal is presented in Section III. In Section IV, the optimal dual sampling rate is discussed. Numerical simulation is presented in Section V, and our custom-designed sampling hardware with phase synchronization and channel calibration is shown in Section VI.

II. Proposed Approach

An overview of the proposed signal acquisition technique utilizing dual-rate (or two-channel) time-interleaved undersampling hardware and associated multicoset signal reconstruction algorithms is shown in Fig. 1. The input test signal is simultaneously, but with different sampling frequencies (f_1, f_2), digitized by two wideband analog-to-digital converters (ADCs) clocked by two individual programmable sampling time-base generators that share a frequency reference oscillator. The two sets of discrete samples obtained from the two uniform samplers are transferred to a digital signal processor (DSP), where they are merged into a single sample set whose sample grid becomes nonuniform. The merged dual-rate samples are digitally classified into p sampling channels, where each sampling channel represents a uniform sample grid with a common sample interval, which is known as a multicoset. Based on the p sets of samples and a *priori* frequency band information of the test signal, a multicoset based signal reconstruction algorithm can be used to solve the linear system of p data sets and recover the original test signal in the frequency-domain as well as in the time-domain with enhanced time/frequency resolution beyond the original hardware sampling rate.

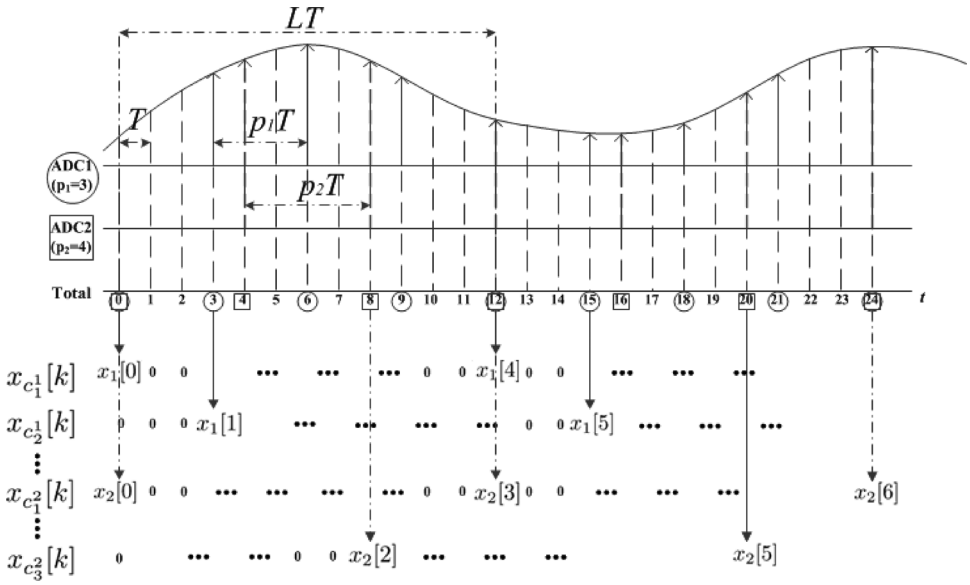

Fig. 2. Samples from ADC_1 ($p_1 = 3$) and ADC_2 ($p_2 = 4$) are converted to multicoset sample sets on the uniform grid with a period $L = 12$.

A. Dual-rate Time-interleaved Undersampling

Let $x(t)$ be a continuous real signal defined over time t and let its continuous-time Fourier transform (CTFT) be

$$X(f) = \int_{-\infty}^{\infty} x(t)e^{-j2\pi ft}dt. \tag{1}$$

We assume that $x(t)$ is a band-limited, multiband signal with known frequency bands. The frequency bands of $x(t)$ are defined as

$$B = \pm \bigcup_{i=1}^{n} [a_i, b_i), \tag{2}$$

where $0 \le a_1 < b_1 \ldots < a_n < b_n$, which we call *active bands*.

It is well-known that a perfect reconstruction of the signal $x(t)$ is achieved by uniformly sampling a band-limited signal with a sampling frequency of $f_{\mathrm{Nyquist}} = 2b_n$, where f_{Nyquist} is the Nyquist rate. In dual-rate time-interleaved undersampling, the signal $x(t)$ is sampled at two different sampling frequencies that are much lower than f_{Nyquist}. $x_1[k]$ and $x_2[k]$ are the discrete samples acquired by sampling the signal $x(t)$ with ADC_1 and ADC_2, whose sampling intervals are T_1 and T_2 respectively. In cases where both the acquired sample sets are phase aligned to a common reference time-base (assuming no relative phase errors), $x_1[k]$ and $x_2[k]$ are expressed as the following

$$\begin{cases} x_1[n] = x(nT_1), \\ x_2[n] = x(nT_2), \end{cases} \quad -\infty < n < \infty \tag{3}$$

where the sampling intervals T_1 and T_2 are selected by using the equation shown below

$$\begin{aligned} T_1 &= p_1 T, \\ T_2 &= p_2 T, \end{aligned} \tag{4}$$

where p_1 and p_2 are *coprime* integers and T denotes the base sampling period (much smaller than T_1 and T_2) that can be *virtually* obtained via the proposed signal reconstruction technique. The discrete-time stamps of the two samplers are given by

$$C_1 = \{c_i^1 \mid c_i^1 = p_1 i : \ 0 \le c_i^1 < L, \ i = 0, 1, \ldots, p_2 - 1\}, \tag{5}$$

$$C_2 = \{c_i^2 \mid c_i^2 = p_2 i : \ 0 \le c_i^2 < L, \ i = 0, 1, \ldots, p_1 - 1\}, \tag{6}$$

where L denotes the least common multiple (LCM) of the two co-prime integers p_1 and p_2, which is $L = p_1 p_2$. A set of total discrete-time stamps containing both C_1 and C_2 is obtained by merging the two sets.

$$C_{\mathrm{total}} = C_1 \cup C_2 = \{c_1, c_2, \ldots, c_{p_{\mathrm{total}}}\},$$

where p_{total} denotes the cardinality of C_{total}, which is $p_1 + p_2 - 1$.

In Fig. 2, an example of the discrete-time stamps for dual-rate sample sets with $p_1 = 3$ and $p_2 = 4$ is illustrated, where a pattern of particular discrete-time stamps repeats every $L(= 12)$ discrete-time stamps. In this example, $C_1 = \{0, 3, 6, 9\}$, $C_1 = \{0, 4, 8\}$, $C_{\mathrm{total}} = \{0, 3, 4, 6, 8, 9\}$, and the discrete-time stamps in C_{total} are *nonuniform*. Note that the pattern of discrete-time stamps in C_{total} is uniquely defined by p_1 and p_2, whose selection scheme is studied in Section IV.

B. Dual-rate-to-multicoset Sample Re-sequencing

Dual-rate sample sets obtained from two distinct sampling rates are digitally converted to multicoset sample sets $(x_{c_i^1}, x_{c_i^2})$ by re-sequencing the raw samples as shown below

$$x_{c_i^1}[k] = \begin{cases} x_1[lp_2 + i - 1], & \text{if } k = lL + c_i^1, l \in \mathbb{Z} \\ 0, & \text{otherwise,} \end{cases} \tag{7}$$

$$x_{c_i^2}[k] = \begin{cases} x_2[lp_1 + i - 1], & \text{if } k = lL + c_i^2, l \in \mathbb{Z} \\ 0, & \text{otherwise,} \end{cases} \tag{8}$$

where $k = 0, 1, 2, \ldots, Ln - 1$. The number of samples in each coset is the same as the number of samples that can be virtually obtained from the base frequency $1/T$ because of zero-padding. Given L and p, the total number of possible cosets is $\frac{L!}{p!(L-p)!} = \binom{L}{p}$. The cyclic distance between the sample points determines the uniqueness of the cosets.

C. Multicoset Signal Reconstruction Algorithm

In this section, we provide a review of multicoset signal reconstruction algorithms [4], [6], which are used for signal reconstruction of the re-sequenced sample cosets provided in Section II-B. In multicoset signal reconstruction, we choose subsamples from the samples of the base frequency, $1/T$. The subsamples are chosen to have a periodic pattern but do not necessarily have a uniform space between them. Then, we can define the sampling locations $(kL + c_i)T$ for any integer k, where L is the period of the sampling pattern, c_i is a positive integer and $0 \leq c_i < L$ for $i = 1, \ldots, p$. We call the set $C = \{c_1, \ldots, c_p\}$ the "cosets".

For a given coset, c_i, the discrete-time sequence that samples the input signal at $(kL + c_i)T$ and zero-pads at the other points is described as

$$x_{c_i}[n] = \begin{cases} x(nT), & n = kL + c_i, \text{where } k \in \mathbb{Z} \\ 0, & \text{otherwise.} \end{cases} \tag{9}$$

The discrete-time Fourier transform (DTFT) of the sequence x_{c_i} is expressed as

$$Y_{c_i}(e^{-j2\pi fT} = \frac{1}{LT} \sum_{r=0}^{L-1} X\left(f + \frac{r}{LT}\right) e^{\frac{j2\pi r c_i}{L}}, \qquad f \in F_0, \tag{10}$$

where $F_0 = [0, \frac{1}{LT})$ and $X(f)$ is the CTFT of $x(t)$ as defined in (1)[1] The right-hand side of (10) describes the spectral aliasing due to the undersampling by L (the summation of the CTFT L times) and the phase-shift due to the time-offset of c_i (the complex exponential at the end of the equation). Note that the sequence x_{c_i} is composed of the c_i discrete-time delayed samples downsampled by a factor of L with $L - 1$ interleaved zeros.

Now, we consider the aliased boundaries of the active bandwidth from (2) defined by the following

$$\Gamma = \bigcup_{i=1}^{n} mod\left(a_i, \frac{1}{LT}\right) \cup \bigcup_{i=1}^{n} mod\left(b_i, \frac{1}{LT}\right) \cup \left\{0, \frac{1}{LT}\right\}, \tag{11}$$

where a_i and b_i are defined as the lower and upper bound of the i-th frequency band in (2). Let the increasing-order elements of the set Γ to be $\{\lambda_0 = 0, \lambda_1, \ldots, \lambda_M = \frac{1}{LT}\}$, and then the frequency interval of the aliased boundaries can be defined as

$$G_m = [\lambda_{m-1}, \lambda_m), \qquad 1 \leq m \leq M - 1. \tag{12}$$

Note that the frequency domain of X_{c_i}, F_0, is divided into M number of subintervals. For each subinterval, define the "spectral index sets" as

[1]The Fourier transforms discussed in this section are CTFT and DTFT. Therefore, the variable f is a continuous variable. Note that the variable f is an unbounded real number in (1), whereas f in (10) is a bounded real number of the bounded set F_0.

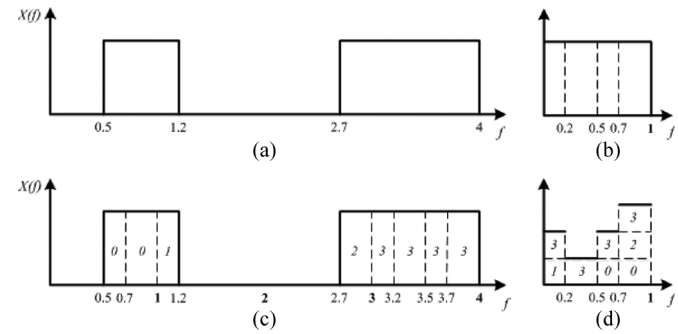

Fig. 3. (a) Active bands of the test signal; (b) Aliased boundaries of active bands (G_m); (c) Active bands are divided into subintervals corresponding to G_m; (d) Spectral index sets (k_m) and their cardinalities (q_m).

$$k_m = \left\{ r | X\left(f + \frac{r}{LT}\right) \subset F, f \in G_m \right\},$$

and their cardinality (the number of element of a set) as $q_m \leq L$. Let $k_m(l)$ denote the l-th element of k_m if k_m is not empty. The spectral index sets indicate which part of the active bandwidth contributes X_{c_i}.

By the definition of the spectral index sets, (10) is reduced as follows

$$\begin{aligned} Y_{c_i}(e^{-j2\pi fT}) = &\frac{1}{LT} X\left(f + \frac{k_m(1)}{LT}\right) e^{\frac{j2\pi k_m(1) c_i}{L}} + \ldots \\ &+ X\left(f + \frac{k_m(q_m)}{LT}\right) e^{\frac{j2\pi k_m(q_m) c_i}{L}}, f \in G_m, \end{aligned}$$

where the RHS is the summation of the $q_m \leq L$ terms, while (10) is that of L terms.

Example: Suppose the input signal bandwidth is given as $B = [0.5, 1.2) \cup [2.7, 4)$ (Fig. 3(a)). Let $L = 12$ and $T = 1/12$. By (11), we obtain $\Gamma = \{0, 0.2, 0.5, 0.7, 1\}$ and $M = 4$ (Fig. 3(b)). The frequency intervals of Γ in (12) are

$$\begin{aligned} G_0 &= [0, 0.2), \quad G_1 = [0.2, 0.5), \\ G_2 &= [0.5, 0.7), \quad G_3 = [0.7, 1). \end{aligned}$$

The spectral index sets and their cardinalities are the follows (Fig. 3(d)):

$$\begin{aligned} k_0 &= \{1, 3\}, & q_0 &= 2, \\ k_1 &= \{3\}, & q_1 &= 1, \\ k_2 &= \{0, 3\}, & q_2 &= 2, \\ k_3 &= \{0, 2, 3\}, & q_3 &= 3. \end{aligned}$$

In summary, (10) is expressed in matrix form as follows

$$\mathbf{y}(f) = \mathbf{A}_m \mathbf{x}_m(f), \qquad f \in G_m, 1 \leq m \leq M, \tag{13}$$

where $\mathbf{y}(f)$ is a p-length vector, $\mathbf{x}_m(f)$ is a q_m-length vector and $\mathbf{A}_m$ is a p-by-q_m matrix. They are defined by the following

$$\begin{aligned} [\mathbf{y}(f)]_i &= Y_{c_i}(e^{-j2\pi fT}), \ i = 1, \ldots, p, \ f \in G_m, \\ [\mathbf{x}_m(f)]_k &= X\left(f + \frac{k_m(k)}{LT}\right), \ k = 1, \ldots, q_m, \ f \in G_m, \\ [\mathbf{A}_m]_{ik} &= \frac{1}{LT} e^{\frac{j2\pi c_i k_m(k)}{L}}. \end{aligned} \tag{14}$$

Each element of the vectors $\mathbf{y}(f)$ and $\mathbf{x}_m(f)$ is a function of a continuous variable $f \in G_m$. Equation (13) can be easily understood by fixing f as any number in G_m. Then, the equation becomes a typical p-by-q_m linear system. In the next section, f is discretized by the Discrete Fourier Transform (DFT). Therefore, f will become a finite-dimension vector and for each element its corresponding linear system will be created.[2] The reconstruction of the original signal is achieved by solving (13) for each m. Depending on the dimensions of $\mathbf{y}$ and $\mathbf{x}_m$ and the rank of $\mathbf{A}_m$, the uniqueness and the existence of the solutions are determined. In general, if $p \geq q_m$ and $\mathbf{A}_m$ is a full column rank matrix, the system is overdetermined, and thus we can apply the Moore-Penrose pseudoinverse to compute a least-square solution to the system.

III. Active Band Detection

In the previous section, the active bands are the a *priori* information for the reconstruction algorithm. For a signal with arbitrary active bands, however, the detection of the active bands is required for the full reconstruction. In this section, the active band sensing algorithm based on the Orthogonal Matching Pursuit (OMP) and asynchronous multirate sampling proposed in [25] is introduced.

The active bands are detected by comparing the aliasing spectra undersampled by two (or more) different sampling frequencies. The aliased spectra by each sampling frequency are unfolded and converted to analog frequencies. The sensing matrix, specially defined as the extended version of the Discrete Fourier Transform (DFT) matrix, projects the undersampled time-domain samples onto a common frequency basis. The common frequency basis is selected to align the two different DFT spectral grids. Once the aliased spectra are compared by the sensing matrices, the frequency support containing the highest energy in both spectra is chosen to be the first detected active band. The detected spectral component is then subtracted from the original waveform. This entire process (conversion, detection and subtraction) is iterated until the energy of the residual waveform reaches the stopping criteria.

The success rate for the detection increases with the number of different sampling rates. Because the algorithm can use asynchronous sample sets, two or more sample sets can be captured ahead of the dual-rated multicoset algorithm to provide more precise band locations.

IV. Dual-rate Sampling Frequency Optimization

Given that the active bands of the test signal are known a *priori*, the optimal combination of the dual sampling rates can be found. In the proposed approach, f_1 is set to the maximum sampling rate (1.2-Gsps) that our custom hardware module can achieve, and f_2 is tuned with 10 MHz resolution to find the optimal sampling frequencies. The optimality of the sampling frequency configuration (for the test signal with particular active bands) is verified by measuring the normalized mean square error (NMSE) of the reconstructed signal. In addition, the performance of signal reconstruction of dual-rate sampling with the optimal sampling frequency configuration is compared to that of the conventional multicoset sampling hardware.

A. Base Frequency

The base sampling rate $1/T$ should be set higher than $f_{\text{Nyquist}} = 2b_n$ to obtain a perfect reconstruction without spectral aliasing. Equation (4) results in a necessary condition for f_b as follows.

$$f_b = \frac{1}{T_b} = p_1 f_1 = p_2 f_2 > f_{\text{Nyquist}}, \tag{15}$$

where $f_1 = 1/T_1$ and $f_2 = 1/T_2$. The base sampling frequency is represented in an exclusive form of f_1 and f_2

$$f_b = \frac{f_1 f_2}{\gcd(f_1, f_2)} > f_{\text{Nyquist}}, \tag{16}$$

where $\gcd(f_1, f_2)$ is the greatest common divisor of f_1 and f_2. Suppose that f_1 and f_2 are any positive integers, and that p_1 and p_2 are coprime integers. If $f_1 p_1 = f_2 p_2$, then $p_1 = \frac{f_2}{\gcd(f_1, f_2)}$ and $p_2 = \frac{f_1}{\gcd(f_1, f_2)}$.

B. Number of Base Samples

The number of base samples N_b is defined as the number of samples in the reconstructed signal represented with the base frequency (or sampling rate) $f_b = 1/T_b$. As shown in Fig. 2, N_b is equal to the number of samples in each re-sequenced coset including zero-padding. In the sampling case shown in (4), $p_2 n$ samples are obtained from ADC_1 and $p_1 n$ samples from ADC_2. Therefore, the number of base samples is determined by

$$N_b = p_1 p_2 n = Ln, \tag{17}$$

and it is regulated with an upper bound. The upper bound constraint is required to efficiently use the memory and computational power of the digital signal processors (DSPs). As each coset occupies N_b, the total number of samples used in estimating a reconstructed signal is $N_b(p_1 + p_2 - 1)$. Note that $\mathbf{y}(f)$ and $\mathbf{x}_m(f)$ in (13) are represented by using the DTFT operation. However, when the algorithm is implemented in the DSP, the discrete Fourier transform (DFT) or fast Fourier transform (FFT) operation must be used. The DTFT of a coset sequence in (10) is approximated by the DFT of N_b samples per coset in the DSP. The total amount of computation required for the DFT operation of all the coset sequences is $(p_1 + p_2 - 1)O(N_b \cdot \log N_b)$.

C. Less Deficient Linear System

The reconstructed spectrum is obtained by solving the system of (13) for $\mathbf{x}_m$. Note that $\mathbf{A}_m$ is the conjugated submatrix of the L-by-L DFT matrix by extracting its rows indexed by the coset (C) and columns indexed by k_m. Though a DFT matrix is a full-rank matrix, its submatrix may not be full-rank.

A key property of sampling patterns that successfully reconstruct the original signal is the Kruskal-rank of the sampling matrix [26]. The Kruskal-rank of $\mathbf{A}$, $\sigma(A)$, is defined as the maximal number k such that every set of k columns of $\mathbf{A}$ is linearly independent. A sampling pattern is called "universal" when the pattern has full Kruskal-rank, i.e., $\sigma(A) = p$. Therefore, a universal sampling pattern simplifies the condition of the uniqueness to $p \geq q_m$. We now address the question of how the

[2]The equations for the linear system will not be explicitly described here because they are exactly the same as (13) and (14) except f is converted to a discrete variable by DFT.

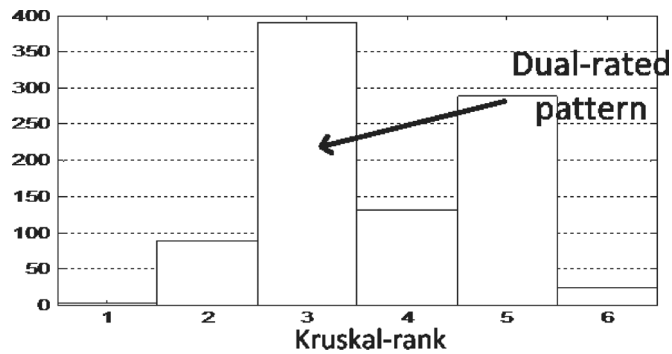

Fig. 4. Kruskal-rank histogram of $L = 12$ and $p = 6$. The Kruskal-rank of the dual-rated pattern, $C = \{0, 3, 4, 6, 8, 9\}$, is 3.

dual-rated pattern is better or worse than the other patterns. As the number of possible patterns is usually very large, a simple case of $L = 12$ and $p = 6$ is chosen for instance. We generated all the possible patterns including the dual-rated pattern $C = \{0, 3, 4, 6, 8, 9\}$ and computed the Kruskal-rank of each pattern. The histogram of the Kruskal-rank is shown in Fig. 4. The figure indicates that the dual-rated pattern may not achieve the universal pattern. Therefore, it is necessary to check the rank of the sampling matrix and verify if the matrix is full-rank.

Moreover, if the number of rows is less than the number of columns, the system is underdetermined, which means the number of solutions is infinite. Therefore, it is desired that the sampling matrix $\mathbf{A}_m$ 1) is full-rank and 2) has more rows than columns. The second statement can be reduced to $p \geq \max_m q_m$. Note that q_m is the cardinality of the spectral index or the number of the overlapped active bandwidth in G_m. It is related to how "sparse" the input signal is. When the input signal is too "broad", there is a higher chance that q_m is a large number. However, the sparsity of the input signal does not directly determine q_m. This is because q_m is determined by LT (the sampling rate of a coset, which decides the amount of spectral fold) as well as the active bandwidth. In this paper, the signal is assumed to be sufficiently sparse that p can outnumber q_m.

Because we assume the rows outnumbers the columns, the sampling matrix is full column rank when $rank(\mathbf{A}_m) = q_m$. Note that the rows and columns of the sampling matrix, A_m, are determined by the sampling pattern (rows) and the spectral index (columns) in (14). Therefore, the rank of the sampling matrix can remain the same or decrease depending on the choice.

As the matrix size varies with the combination, it is not proper to evaluate the rank of the sampling matrix as the objective function. In this case, it is more convenient to see how far the rank of the matrix is from the full rank, i.e., the deficiency of the system. The deficiency of the overall system is defined as

$$D(f_1, f_2) = \sum_{m=1}^{m=M} \left[q_m - rank(\mathbf{A}_m)\right]. \tag{18}$$

When all M subsystems are full column rank, D is 0. Otherwise, the amount of deficiency is stacked over the subsystems.Therefore, we choose a combination of f_1 and f_2 that minimizes D.

TABLE I
INPUT TEST SIGNALS FOR NUMERICAL SIMULATION

Band (GHz)	Mod. Type	f_c (GHz)	Mod. rate	Mod. dev
$[0.25, 0.33]$	AM	0.29	39 MHz	NA
	FM	0.29	50 kHz	20 MHz
	SSB(upper)	0.315	5 MHz	NA
$[1.95, 2.15]$	FM	1.965	1 MHz	5 MHz
	FM	2.02	50 kHz	20 MHz
	FM	2.056	50 kHz	6 MHz
	FM	2.09	50 kHz	18 MHz
	FM	2.136	200 kHz	10 MHz
$[6.00, 6.15]$	PM	6.005	1 MHz	0.1 rad
	FM	6.043	1 MHz	1 MHz
	PM	6.09	10 MHz	0.3 rad
	PM	6.145	1 MHz	0.3 rad

V. NUMERICAL SIMULATION

Via numerical simulation, we compare the reconstructed signal obtained from the optimal sampling (as discussed in Section IV) with that from non-optimal sampling. The test signal consists of various modulated signals (amplitude modulation (AM), single-side band modulation (SSB), frequency modulation (FM) and phase modulation (PM)) with different carrier frequencies (f_c's). Table I summarizes the test signal specification. The test signal also includes Gaussian white noise. The first sampling frequency is fixed at 1.2 GHz, which is the maximum sampling frequency of the hardware and the second sampling frequency is swept under 1.2 GHz.

Before running the dual-rate multicoset algorithm, the asynchronous active band detection from Section III is performed. Three different sampling rates (1.2 GHz, 1.15 GHz, and 1.104 GHz) and 1400 samples for each sample set are used to detect the active bands. As a result, three active bands are detected;[251 MHz–329.1 MHz], [1959.9 MHz–2148.3 MHz], and [6004.3 MHz–6148.2 MHz].

The base sampling rates corresponding to the second sampling rates are shown in Fig. 5(a). The minimum sampling rate required to reconstruct the signal without aliasing is $f_{Nyquist} = 2b_n = 12.3$ GHz. The red horizontal line indicates the minimum sampling rate. The effective numbers of samplings given that each ADC collects $16 \cdot 1024$ samples are shown in Fig. 5(b). To conserve the memory and computational resources, the maximum effective number of samples is limited to $5 \cdot 10^5$. The red horizontal line indicates the maximum effective number of samples. The rank deficiency, $D(f_1, f_2)$, is plotted in Fig. 5(c). This cost function can be calculated by the given active frequency bands of the input signal and the two sampling rates. Thus, the cost function can be obtained before reconstruction of the signal. The normalized mean-squared-error (NMSE) is shown in Fig. 5(d). The NMSE is defined as the squared error between the DFT by the uniform sampling at the base frequency and the reconstructed DFT by the proposed algorithm.

Spectral aliasing (including overlapping) is shown in Fig. 6 as an example. A single spectrum itself by a single sampling rate is undersampled. Hence, the spectrum is aliased, and in the worst case it can be overlapped. In the previous multirate works ([8], [25]), the overlapped spectrum could not be unscrambled, whereas the multicoset algorithm can reconstruct the original spectrum under the condition discussed

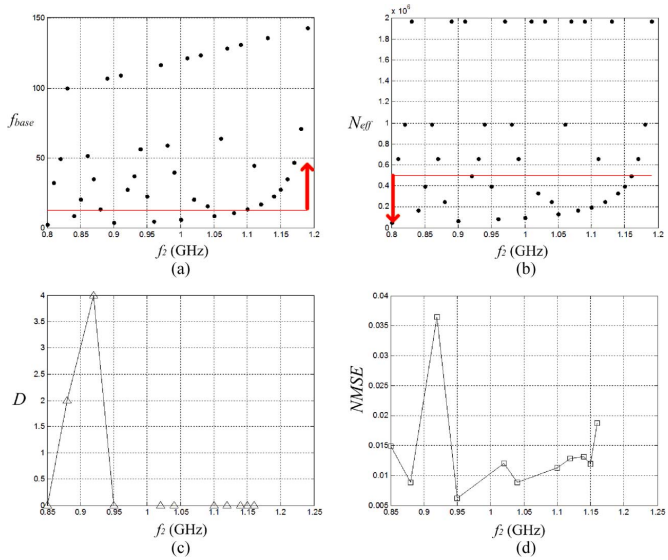

Fig. 5. (a) The base frequency over f_2. (b) The effective number of sampling over f_2. (c) The objective function over f_2. (d) The NMSE over f_2.

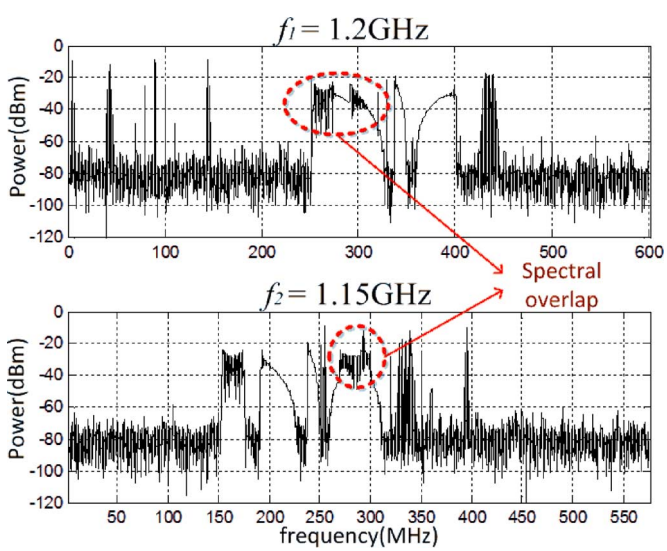

Fig. 6. Aliased and overlapped spectra sampled at dual-rates ($f_1 = 1.2$ GHz, $f_2 = 1.15$ GHz).

in Section IV-C. In Fig. 7, the reconstructed spectra of a non-optimal case ((a), $f_2 = 0.92$ GHz, $D = 4$)and an optimal case ((b), $f_2 = 1.15$ GHz, $D = 0$) are compared. The reconstructed spectrum (red) and the original spectrum by uniform sampling at the base frequency (black) are plotted to visualize the amount of reconstruction error. It is notable that significant reconstruction errors are presented in the non-optimal case. In contrast, the reconstructed spectrum in optimal case matches well with the original spectrum. In both cases, the noise floor is increased by the noise component outside the active bandwidth.

VI. Hardware Validation: Dual-rate Time-interleaved Undersampling

The proposed dual-rate time-interleaved undersampling scheme was implemented in two hardware modules: a dual-rate analog-to-digital converter (ADC) module and a digital data acquisition module, as shown in the block diagram in Fig. 8. The dual-rate ADC module acquires the input analog signal at dual sampling rates to generate nonuniform periodic digital samples. The obtained digital sample data are transferred through high-speed multi-pin connectors to the digital data acquisition module, which stores the sample data in memory for digital post-processing that is performed offline.

In Fig. 8, the signal acquisition paths are denoted by solid lines. The input analog signal is divided in power by a wideband power splitter. The divided signals are individually fed to wideband track-and-hold (T/H) amplifiers. These T/H amplifiers are used as an analog front-end of the dual-rate ADC module and help increase the overall analog bandwidth beyond the given input bandwidth of the ADCs being used (ADC12D1800, Texas Instruments) by sampling/holding the signal at the front-end with minimal signal distortion. The high-speed 12-bit ADCs are able to operate with a sampling clock with a frequency of up to 1.8 GHz and to cover a 3 GHz input bandwidth (when the T/H amplifier is not used as an analog front-end). The ADCs acquire the signal in the hold mode at the output of the T/H amplifiers.

We choose two different models of the T/H amplifier with different input bandwidths on purpose to create gain/phase mismatch between the divided signal paths as shown in Fig. 8. The T/H amplifier used for the upper channel (HMC5641BLC4B, Hittite) has 5 GHz of bandwidth, and the T/H amplifier for the lower channel (HMC5640BLC4B, Hittite) has 18 GHz of bandwidth. A compensation technique for gain/phase mismatch is described in Section VI-B. The digitized samples obtained by the combination of T/H amplifiers and ADCs are collected by a field-programmable gate array (FPGA) mounted on the digital data acquisition module.

The sampling time-base (or clock) paths are denoted by dashed lines in Fig. 8. A 100 MHz crystal oscillator is used as a common frequency source for the sampling time-base of the ADCs as well as the system clock of the onboard FPGA (Spartan 6, Xilinx). To alleviate concerns regarding jitter noise of the reference oscillator, which might increase the sampling noise of the ADCs, we use a clock conditioner (LMK040033BISQ, National Semiconductor) to reduce the unwanted jitter component of the reference oscillator. Based on the reference frequency of the conditioned clock source, two programmable frequency synthesizers (LMX2541SQ3320E, National Semiconductor) generate high-frequency sampling time-bases for the two ADCs. Before being provided to the ADCs, the sampling clock signals are time-delayed by dedicated delay components (HMC856LC5, Hittite), which are used to control the relative delay of the two sampling clocks for a debugging purpose. The onboard FPGA controls and programs these mixed-signal components in the dual-rate ADC module. Pictures of the dual-rate ADC module and the digital data acquisition module are shown in Fig. 9.

A. Sampling Phase Synchronization

The dual-rate-to-multicoset sample re-sequencing described in Section II-B assumes no relative sampling phase offset between the initial sampling phases of the dual-rate sample sets. In such an ideal case, the initial sampling phases of the two data sets should be aligned at in exactly the same phase. However,

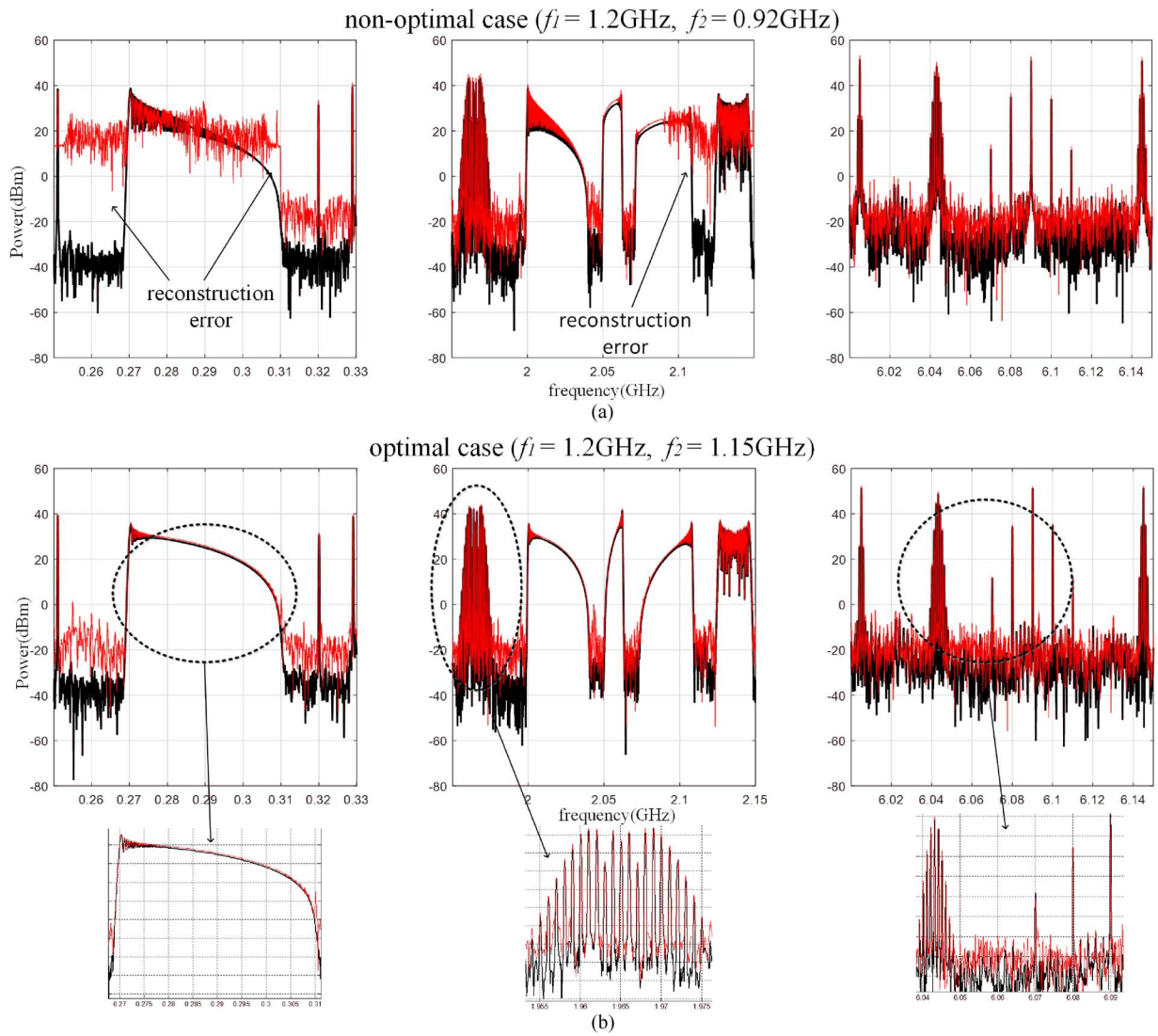

Fig. 7. Comparison between the original spectrum (black) and the reconstructed spectrum (red) with a non-optimal and an optimal combination.

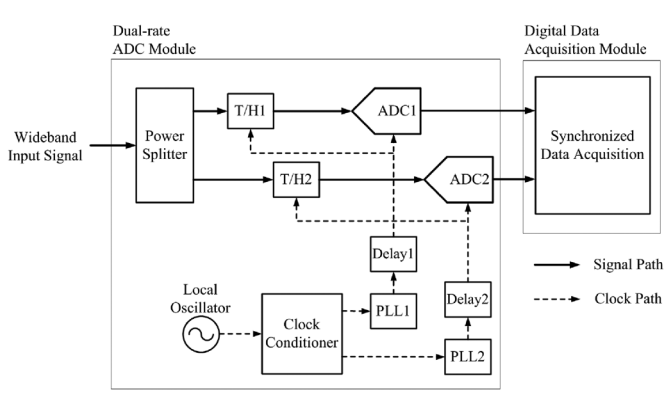

Fig. 8. Block diagram of the proposed dual-rate time-interleaved undersampling hardware consisting of two hardware modules: the dual-rate ADC module and the digital data acquisition module.

in practice, the amount of phase offset varies depending on the arrival time of the trigger signal initiating data acquisition. This random phase offset occurs due to the asynchronous trigger time with the dual-rate sampling frequency.

We propose an empirical method for phase-synchronizing dual-rate sample data sets. A potential phase offset (due to a potential timing mismatch between either the signal acquisition paths or the sampling time-base paths) between two sets of the obtained signal samples with different sampling rates is not constant over the data acquisiton period. Due to this fact, the phase alignment of the two sample sets is not a simple task.

In the digital data acquisition module, the digital sample sets transferred from the dual-rate ADC module are deserialized and fed to FIFO logics implemented in the FPGA. To prevent uncertainty in the amount of phase offset, we implemented a synchronization logic associated with the FIFOs and deserializers. Using the fact that the relative phase between the two clocks is periodic with every p_2 of the first clock (or every $p1$ of the second clock), the trigger signal is synchronized with an edge-detecting counter of the first clock. This trigger mechanism forces the write-enable of the FIFO to be issued on a certain phase relationship. The FPGA logic diagram is shown in Fig. 10, where $f_1 = 1.2$ GHz and $f_2 = 1.15$ GHz. The ADC12D1800 outputs the data at half the sampling rate on

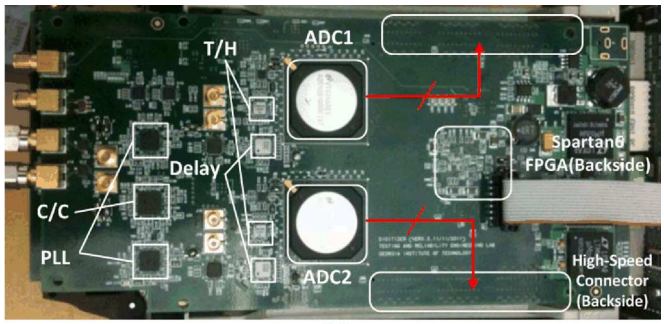

(a)

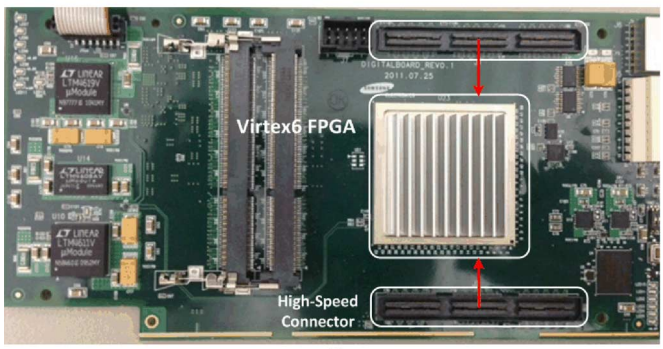

(b)

Fig. 9. (a) Picture of the dual-rate ADC module. (b) Picture of the digital data acquisition module.

twice the number of buses. The output data are deserialized by 1-to-4 DDR SERDES of Virtex6 in the digital data acquisition module. Then, the deserialized data are stored in the FIFO. Therefore, the phase offset between the two data sets is determined by the write-enable of the FIFO. Note that the trigger signal is synchronized with one of the sampling clocks. The counter holds the trigger signal until the current state is equal to p_2.

B. Calibration—Mismatch Compensation

Gain/phase mismatch between the two data acquisition channels (including T/H amplifiers and ADCs) is not negligible in cases where wideband signal acquisition is performed. Associated signal distortion needs to be compensated for prior to the signal reconstruction. The types of mismatch we consider are frequency-dependent gain and phase mismatches. These mismatches potentially result from channel delay skew and chip-to-

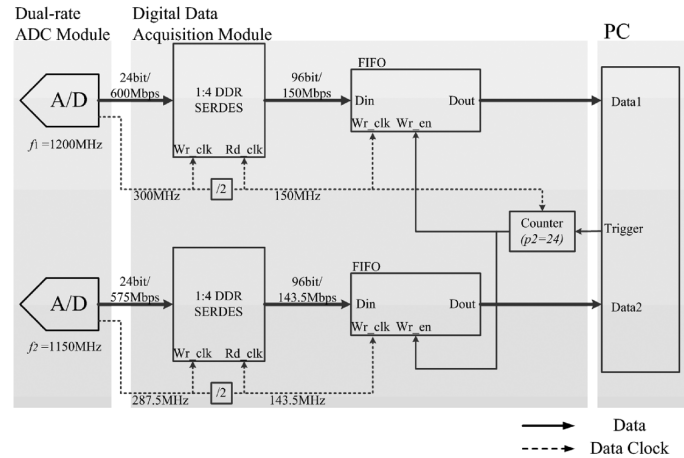

Fig. 10. FPGA logic diagram of the digital data acquisition module.

chip performance variation of ADCs and T/H amplifiers. In this section, the second signal acquisition channel is considered a reference channel for simplicity. The channel mismatch, $F(f)$, is defined as

$$X_1(f) = F(f)X_2(f), \tag{19}$$

where $X_1(f)$ and $X_2(f)$ are the continuous Fourier Transform of the input signal of ADC_1 and ADC_2 respectively, and $F(f)$ is the frequency response of the first signal acquisition channel when the second channel is assumed to be ideal.

The mismatch compensation terms are applied to (13), and $m = 1$ is assumed for simplicity. Equation (13) can be separated into two channels as shown in (20), see (20) shown at the bottom of the page.

The diagonal element $F_i = |F_i|e^{j\phi_i}$ represents the approximated piecewise gain ($|F_i|$) and phase (ϕ_i) mismatch of $F(f)$ where $\frac{k(i)}{LT} \le f < \frac{k(i)+1}{LT}$. Note that the rank of the new system matrix AQ remains the same because Q is full column rank. Therefore, as long as the original system matrix A is of full column rank, the least-square solution of $\mathbf{x}$ is still achieved by the pseudo-inverse of AQ.

The mismatch matrix F can be found by applying a known single-tone test signal to the two signal acquisition channels and measuring the gain and phase offset between the channels in the digital signal post-processing. As the input signal and the sampling clock are not synchronized, the spectral leakage prevents

$$\underbrace{\begin{bmatrix} Y_{c_0^1} \\ \vdots \\ Y_{c_{p_2-1}^1} \\ Y_{c_0^2} \\ \vdots \\ Y_{c_{p_1-1}^2} \end{bmatrix}}_{\mathbf{y}(f)} = \frac{1}{LT} \underbrace{\begin{bmatrix} e^{j2\pi c_0^1 k(1)} & e^{j2\pi c_0^1 k(2)} & \cdots & e^{j2\pi c_0^1 k(q)} \\ \vdots & \vdots & \ddots & \vdots \\ e^{j2\pi c_{p_2-1}^1 k(1)} & e^{j2\pi c_{p_2-1}^1 k(2)} & \cdots & e^{j2\pi c_{p_2-1}^1 k(q)} \\ e^{j2\pi c_0^2 k(1)} & e^{j2\pi c_0^2 k(2)} & \cdots & e^{j2\pi c_0^2 k(q)} \\ \vdots & \vdots & \ddots & \vdots \\ e^{j2\pi c_{p_1-1}^2 k(1)} & e^{j2\pi c_{p_1-1}^2 k(2)} & \cdots & e^{j2\pi c_{p_1-1}^2 k(q)} \end{bmatrix}}_{\mathbf{A}} \underbrace{\begin{bmatrix} F_1 & \cdots & 0 \\ \vdots & \ddots & \vdots \\ 0 & \cdots & F_q \\ 1 & \cdots & 0 \\ \vdots & \ddots & \vdots \\ 0 & \cdots & 1 \end{bmatrix}}_{\mathbf{Q}} \underbrace{\begin{bmatrix} X\left(f + \frac{k(1)}{LT}\right) \\ X\left(f + \frac{k(2)}{LT}\right) \\ \vdots \\ X\left(f + \frac{k(q)}{LT}\right) \end{bmatrix}}_{\mathbf{x}(f)}, \quad f \in G. \tag{20}$$

an accurate estimation. A fractional DFT basis is used to estimate the fundamental frequency of the input signal. This method is used to fold back the samples over the fundamental period of the input signal, and then the nonuniform DFT is performed to evaluate the gain and phase for the samples from each ADC.

The nonuniform DFT basis for the fundamental frequency can be defined as

$$\mathbf{v} \equiv \frac{1}{\sqrt{N}} \left[e^{-j2\pi t_d[0]/N} \; e^{-j2\pi t_d[1]/N} \; e^{-j2\pi t_d[2]/N} \; \ldots \; e^{-j2\pi t_d[N-1]/N} \right]^T, \quad (21)$$

where $t_d[k]$ is the time-location of the $(k-1)$th sample. Then, the gain mismatch and the phase mismatch in $[\frac{k(i)}{LT}, \frac{k(i)+1}{LT})$is described as

$$|F_i| = \frac{|\mathbf{v} \cdot \mathbf{x_1}|}{|\mathbf{v} \cdot \mathbf{x_2}|}, \quad (22)$$

$$\phi_i = arg(\mathbf{v} \cdot \mathbf{x}_1) - arg(\mathbf{v} \cdot \mathbf{x}_2), \quad (23)$$

where $\mathbf{x}_1$ and $\mathbf{x}_2$ are the samples from ADC1 and ADC2 for the corresponding subband.

The reasonable frequency for the single-tone test signal will be at half of its range, $f_m = \frac{k(i)}{LT} + \frac{1}{2LT}$. However, the simple frequency relationship between the test signal (f_t) and the sampling clock (f_s) does not generate fine resolution for $t_d[k]$. For example, if $f_t = \frac{f_s}{3}$, the time sequence $t_d[k]$ will be clustered into only three sample points, which is not sufficient to evaluate the gain and phase of the input signal. In other words, if the test signal and the sampling clock are related by

$$f_t = \frac{N}{M} f_s, \quad (24)$$

where N and M are coprime integers, then the time sequence $t_d[k]$ is clustered into M number of sets. Therefore, the frequency of the test signal will be tuned so that both M is sufficiently large and f_t is close to f_m.

To evaluate the proposed mismatch compensation technique, we apply a known single-tone test signal to the signal acquisition channels of the dual-rate ADC module. The sampling frequencies of the two ADCs are fixed at 1.2 GHz (no dual-rate sampling is required for calibration), and the frequency of the test signal is set to have the $M = 997$ frequency relationship shown in (24). Fig. 11 shows the waveforms reconstructed from the samples obtained from each ADC containing gain/phase mismatch. Compared to Fig. 11(a), a significant gain mismatch is observed in Fig. 11(b) because the bandwidth of the T/H amplifier used for the first signal acquisition channel is set to ≈5 GHz on purpose. The frequency components of the test signal and the associated gain/phase mismatch measured in hardware experiments are listed in Table II.

C. Evaluation

The frequency components of the multiband test signal defined in Table III are individually generated by RF signal generators (Agilent E4432B, E8257D) and combined with wideband power combiners. The generated test signal is fed to the signal acquisition module for dual-rate undersampling and the proposed signal reconstruction. Three different sampling rates

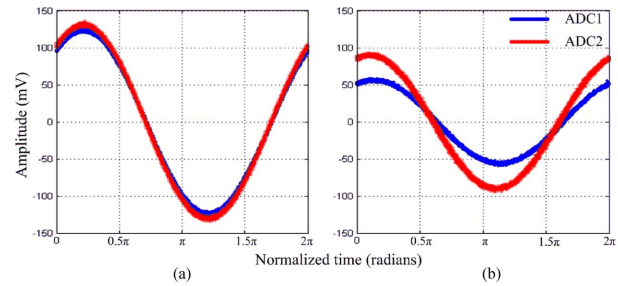

Fig. 11. The signal reconstruction by fundamental frequency estimation for the test signal at (a) 275.6269 MHz and (b) 6025.276 MHz.

TABLE II
MISMATCH MEASUREMENT RESULT

f_t (MHz)	f_m (MHz)	$\|F_i\|$	ϕ_i (rad)
275.6269	275	0.9421	-0.0074
324.9749	325	0.9406	-0.0105
1975.125	1975	0.9130	0.0563
2024.473	2025	0.9129	0.0548
2075.025	2075	0.9154	0.0622
2124.373	2125	0.9154	0.0666
6025.276	6025	0.6237	-0.0918
6074.624	6075	0.6239	-0.0909
6125.176	6125	0.6229	-0.1078

TABLE III
INPUT TEST SIGNALS FOR HARDWARE MEASUREMENT

Band (GHz)	Mod. type	f_c (GHz)	Dev. (MHz)	Rate (MHz)
$[0.25, 0.33]$	Single tone	0.3	NA	NA
$[1.95, 2.15]$	FM	2.06	6	0.05
$[6.00, 6.15]$	FM	6.04	1	1

(1.2 GHz, 1.15 GHz, and 1.104 GHz) and 1400 samples for each sample set are used to detect the active bands. As a result, three active bands are detected;[294 MHz–308 MHz], [2041 MHz–2068 MHz], and [6038 MHz–6048 MHz]. We determine the optimal sampling frequencies as 1.2 GHz and 1.15 GHz, as described in Section IV, for the frequency contents of the test signal shown in Table III. In this configuration, the bandwidth of the sub-band is $1/LT = 50$ MHz. In Fig. 12, the signal reconstruction without using the mismatch compensation technique (a) is compared to the waveform with compensation (b). The performance of the signal reconstruction without gain/phase mismatch compensation is significantly degraded because the channel mismatch is considerable in wideband signal acquisition, especially in the third band of the test signal. The test result shows that the mismatch compensation is necessary for the quality of signal reconstruction.

In Fig. 13, each spectrum of the multiband test signal is individually measured with a spectrum analyzer (HP E4407B) for comparison with the signal reconstructed by the proposed signal acquisition technique. The three measured frequency bands of the test signal are shown in Fig. 13(a), (b) and (c), where the frequency span is 30 MHz, and the frequency resolution is set to 100-kHz.

The third band of the test signal with frequency modulation (FM) is chosen for a closer look and for comparison between the spectrum measurement and the proposed signal acquisition. The spectrum analyzer measurement and the proposed dual-

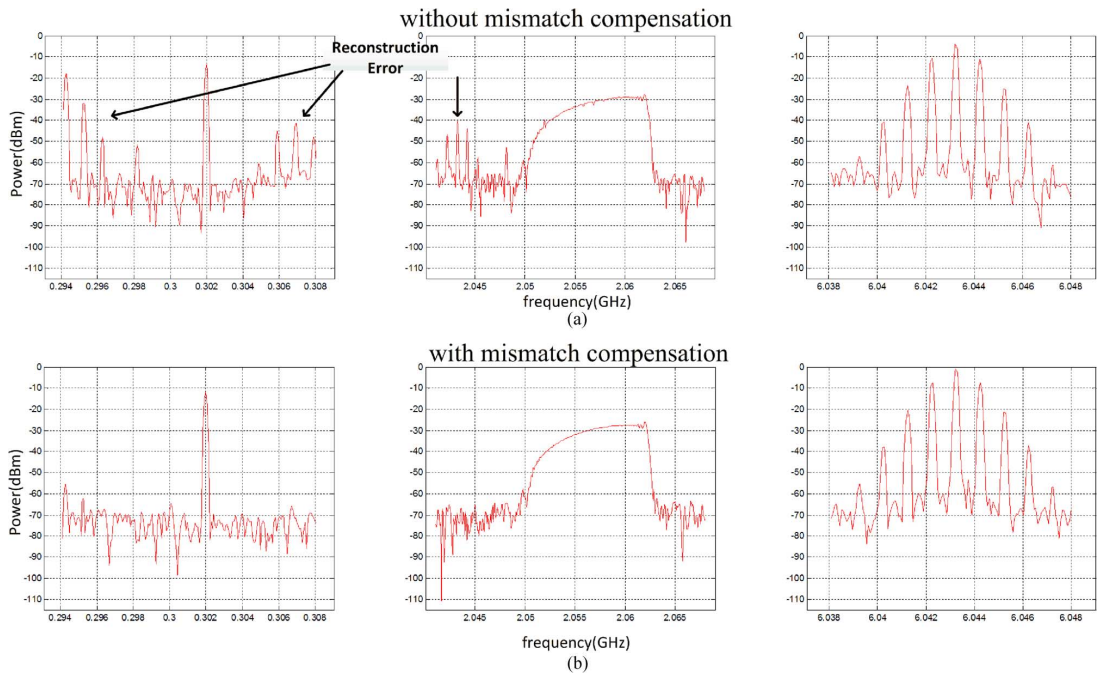

Fig. 12. Signal reconstruction (a) without mismatch compensation and (b) with mismatch compensation.

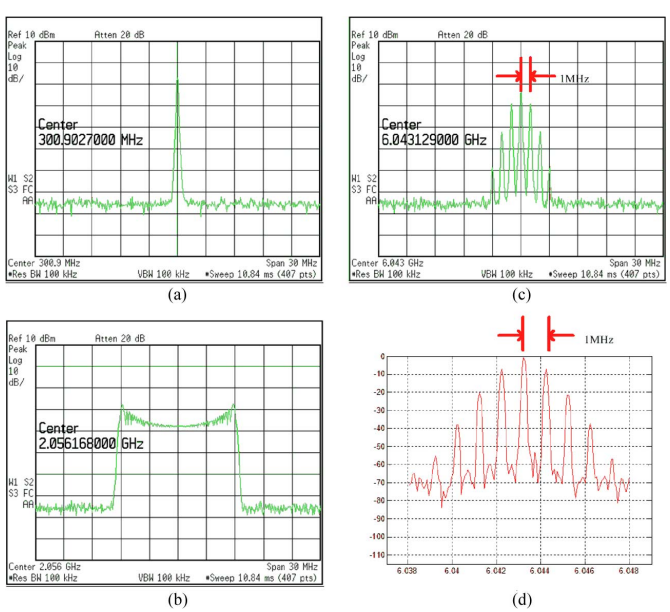

Fig. 13. Comparison between the spectrum analyzer measurements, (a), (b) and (c), and the proposed dual-rate undersampling measurement, (d).

rate time-interleaved undersampling based measurement of the same FM test signal are shown in Fig. 13(c) and Fig. 13(d), respectively. As the FM rate of the test signal is 1 MHz, the spectra measured with the spectrum analyzer (shown in Fig. 13(c)) contain a carrier component and an infinite set of side frequencies located symmetrically around the carrier frequency with the spacing of 1 MHz. The spectrum obtained with the proposed sampling approach (shown in Fig. 13(d)) resolves the frequency spacing as well as the measurement of the spectrum analyzer does.

VII. Conclusion

For measurement and reconstruction of a wideband sparse signal, we have proposed a new undersampling signal acquisition technique composed of dual-rate sampling hardware and a multicoset signal processing algorithm. Because of a frequency offset of the dual-rate sampling, nonuniform periodic samples for multicoset algorithms are acquired without many sampling channels. We have derived an explicit equation that converts dual-rate sample sets into multicoset sample sets. As the configuration of the multicoset algorithm varies with the dual-rate sampling frequency, the optimal combination of the dual sampling rates is studied. The optimality of the sampling frequency configuration is verified by computer simulation. For hardware validation, the dual-rate sampling hardware is implemented. We present and solve the issues (phase synchronization and mismatch calibration) on the dual-rate sampling hardware. Hardware results are provided to demonstrate the performance of the proposed method compared to a commercial spectrum analyzer.

Acknowledgment

We are also thankful to Prof. Justin Romberg of Georgia Tech for his insightful comments on this research.

References

[1] M. Mishali, Y. C. Eldar, O. Dounaevsky, and E. Shoshan, "Xampling: Analog to digital at sub-nyquist rates," *IET*, vol. 5, no. 1, pp. 8–20, Jan. 2011.

[2] M. Mishali and Y. C. Eldar, "Blind multi-band signal reconstruction: compressed sensing analog signals," *IEEE Trans. Signal Process.*, vol. 57, no. 3, pp. 993–1009, Mar. 2009.

[3] M. F. Duarte and Y. C. Eldar, "Structured Compressed Sensing: From Theory to Applications," *IEEE Trans. Signal Process.*, vol. 59, no. 9, pp. 4053–4085, Sep. 2011.

[4] R. Venkataramani and Y. Bresler, "Perfect reconstruction formulas and bounds on aliasing error in sub-nyquist nonuniform sampling of multiband signals," *IEEE Tran. Inf. Theory*, vol. 46, no. 6, pp. 2173–2183, Sep. 2000.

[5] M. F. Duarte and R. G. Baraniuk, "Recovery of frequency-sparse signals from compressive measurements," in *Proc. Allerton Conf. Commun., Contr., Comput.*, 2010, pp. 599–606.

[6] R. Venkataramani and Y. Bresler, "Optimal sub-nyquist nonuniform sampling and reconstruction for multiband signals," *IEEE Tran. on Signal Processing*, vol. 49, no. 10, pp. 2301–2313, Oct. 2001.

[7] S. Bourguignon, "A sparsity-based method for the estimation of spectral lines from irregularly sampled data," *IEEE J. Sel. Topics Signal Process.*, vol. 1, no. 4, pp. 575–585, Nov. 2007.

[8] M. Fleyer, A. Linden, M. Horowitz, and A. Rosenthal, "Multirate synchronous sampling of sparse multiband signals," *IEEE Trans. Signal Process.*, vol. 58, no. 3, pp. 1144–1156, Feb. 2010.

[9] Y. Bresler, "Spectrum-blind sampling and compressive sensing for continuous-index signals," *Inf. Theory Appl. Workshop*, Jan. 2008.

[10] J. Selva, "Regularized sampling of multiband signals," *IEEE Trans. Signal Process.*, vol. 57, no. 3, pp. 993–1009, Mar. 2009.

[11] G. Hennenfent and F. Herrmann, "Simply denoise: Wavefield reconstruction via jittered undersampling," *Geophysics*, vol. 73, p. V19, 2008.

[12] J. Laska, S. Kirolos, Y. Massoud, and R. Baraniuk, "Random sampling for analog-to-information conversion of wideband signals," presented at the IEEE Dallas Circuits Systems Workshop (DCAS), Dec. 2006.

[13] J. Tropp, J. N. Laska, M. F. Duarte, J. K. Romberg, and R. G. Baraniuk *et al.*, "Beyond nyquist: Efficient sampling of sparse bandlimited signals," *IEEE Trans. Inf. Theory*, vol. 56, no. 1, pp. 520–544, Jan. 2010.

[14] A. Bruckstein, D. Donoho, and M. Elad, "From sparse solutions of systems of equations to sparse modeling of signals and images," *SIAM Rev.*, Jan. 2009.

[15] A. Rosenthal, A. Linden, and M. Horowitz, "Multirate asynchronous sampling of sparse multiband signals," *JOSA A*, vol. 25, no. 9, pp. 2320–2330, 2008.

[16] Y. C. Pati, R. Rezaiifar, and P. Krishnaprasad, "Orthogonal matching pursuit: Recursive function approximation with applications to wavelet decomposition," in *Proc. 27th Asilomar Conf. Signals, Syst., Comput. Conf.*, 1993, pp. 40–44, IEEE.

[17] S. G. Mallat and Z. Zhang, "Matching pursuits with time-frequency dictionaries," *IEEE Trans. Signal Process.*, vol. 41, no. 12, pp. 3397–3415, Dec. 1993.

[18] S. Chen and D. Donoho, "Basis pursuit," in *Proc. 28th Asilomar Conf. Signals, Syst., Comput. Conf.*, 1994, vol. 1, pp. 41–44.

[19] S. S. Chen, D. L. Donoho, and M. A. Saunders, "Atomic decomposition by basis pursuit," *SIAM J. Sci. Comput.*, vol. 20, no. 1, pp. 33–61, 1998.

[20] M. Wakin, S. Becker, E. Nakamura, M. Grant, E. Sovero, D. Ching, J. Yoo, J. Romberg, A. Emami-Neyestanak, and E. Candes, "A nonuniform sampler for wideband spectrally-sparse environments," *IEEE J. Emerg. Sel. Topics Circuits Syst.* , vol. 2, no. 3, pp. 516–529, Sep. 2012.

[21] M. Mishali, Y. C. Eldar, and A. J. Elron, "Xampling: Signal acquisition and processing in union of subspaces," *IEEE Trans. Signal Process.*, vol. 59, no. 10, pp. 4719–4734, Oct. 2011.

[22] F. Chen, A. P. Chandrakasan, and V. M. Stojanovic, "Design and analysis of a hardware-efficient compressed sensing architecture for data compression in wireless sensors," *IEEE J. Solid-State Circuits*, vol. 47, no. 3, pp. 744–756, Mar. 2012.

[23] G. Leus and D. D. Ariananda, "Power spectrum blind sampling," *IEEE Signal Process. Lett.*, vol. 18, no. 8, pp. 443–446, Aug. 2011.

[24] M. Mishali and Y. C. Eldar, "From theory to practice: Sub-nyquist sampling of sparse wideband analog signals," *IEEE J. Sel. Topics Signal Process.* , vol. 4, no. 2, pp. 375–391, Apr. 2010.

[25] N. Tzou, D. Bhatta, B. J. Muldrey Jr, T. Moon, X. Wang, H. Choi, and A. Chatterjee, "Low cost sparse multiband signal characterization using asynchronous multi-rate sampling: Algorithms and hardware," *J. Electron. Testing*, vol. 31, no. 1, pp. 85–98, 2015.

[26] J. B. Kruskal, "Three-way arrays: Rank and uniqueness of trilinear decompositions, with application to arithmetic complexity and statistics," *Linear Algebra Appl.*, vol. 18, no. 2, pp. 95–138, 1977.

Thomas Moon (S'14–M'14) received the B.S. degree in electrical electronic engineering from Pohang University of Science and Technology (POSTECH), Pohang, Korea, in 2008, and the M.S. degree in electrical and computer engineering from Georgia Institute of Technology, Atlanta, in 2012, where he is currently pursuing the Ph.D. degree. He is currently working as a Graduate Research Assistant with the Testing and Reliability Engineering Group, Georgia Institute of Technology. His current research interests include high-speed signal testing and characterization, signal integrity, and signal reconstruction by undersampling algorithm.

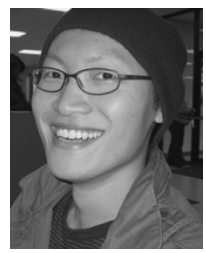

Hyun Woo Choi (S'06–M'11) received the B.S. degree in electrical engineering from Korea University, Seoul, Korea, in 2004, and the Ph.D. degree in electrical and computer engineering from the Georgia Institute of Technology, Atlanta, GA, USA, in 2010. He is a Senior Engineer at Nvidia Corporation, Santa Clara, CA, USA, and an Adjunct Faculty Member with the School of Electrical and Computer Engineering, Georgia Tech. His current research interests include design-for-test, built-in self-test, diagnostics and physical characterization of advanced silicon and post-silicon devices.

Nicholas Tzou was born in Atlanta, Georgia. He grew up in Taipei, Taiwan and received the B.S. degree in Electrical Engineering from National Taiwan University, Taipei, Taiwan, in 2009. He was a Research Assistant with the Testing and Reliability Engineering Lab and worked under supervision of Dr. Abhijit Chatterjee. He received his Ph.D. degree in Electrical and Computer Engineering at Georgia Institute of Technology in 2014. His research interest includes signal processing and hardware-software codesign.

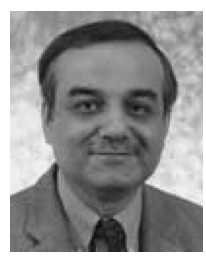

Abhijit Chatterjee (M'83–SM'94–F'07) is a professor in the School of Electrical and Computer Engineering at Georgia Tech and a Fellow of the IEEE. He received his Ph.D. in electrical and computer engineering from the University of Illinois at Urbana-Champaign in 1990. Dr. Chatterjee received the NSF Research Initiation Award in 1993 and the NSF CAREER Award in 1995. He has received six Best Paper Awards and three Best Paper Award nominations. His work on self-healing chips was featured as one of General Electric's key technical achievements in 1992 and was cited by the Wall Street Journal. In 1995, he was named a Collaborating Partner in NASA's New Millennium project. In 1996, he received the Outstanding Faculty for Research Award from the Georgia Tech Packaging Research Center, and in 2000, he received the Outstanding Faculty for Technology Transfer Award, also given by the Packaging Research Center. In 2007, his group received the Margarida Jacome Award for work on VIZOR: Virtually Zero Margin Adaptive RF from the Berkeley Gigascale Research Center (GSRC).